Title
LIMITED ANGLE 3-D RECONSTRUCTIONS FROM CONTINUOUS AND PINHOLE PROJECTIONS

Author
Tam, K.C.

Publication Date
1979-10-01

Lawrence Berkeley Laboratory
UNIVERSITY OF CALIFORNIA

Physics, Computer Science & Mathematics Division

Submitted to IEEE Transactions in Nuclear Science

LIMITED ANGLE 3-D RECONSTRUCTIONS FROM CONTINUOUS AND PINHOLE PROJECTIONS

K. C. Tam, V. Perez-Mendez and B. Macdonald

October 1979

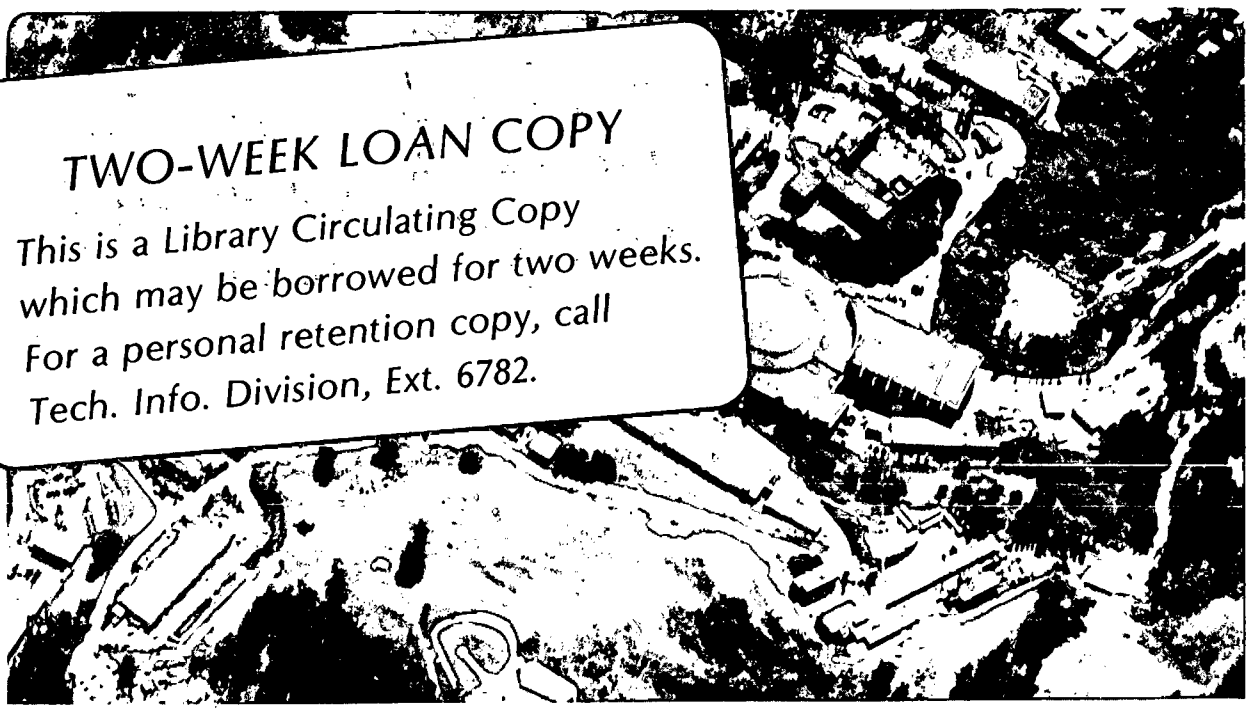

Prepared for the U.S. Department of Energy under Contract W-7405-ENG-48

DISCLAIMER

LIMITED ANGLE 3-D RECONSTRUCTIONS FROM CONTINUOUS AND PINHOLE PROJECTIONS

K. C. Tam, V. Perez-Mendez and B. Macdonald
Lawrence Berkeley Laboratory, Berkeley
and Radiology Department, U.C. San Francisco

Abstract

The propagation of errors incurred in 3-D reconstructions with limited angular input performed by deconvolution and matrix inversion algorithms is analyzed. The convergence rate and noise properties of an iterative scheme that utilizes the finite extent of the object to recover the missing Fourier components in deconvolution are studied. Methods are developed to stabilize the performance of the reconstruction algorithms in the presence of noise. An analysis is given for the necessary condition for complete reconstruction in imaging situations involving a number of discrete inputs confined to limited angular range.

Introduction

Most emission and transmission imaging methods involve taking data in a continuous range of angles or series of discrete angles, as shown in Figs. 1 and 2. The problem of reconstructing the object distribution $\rho(\underline{r})$ from the data is to solve the integral equation

$$\phi(\underline{r}) = \int \rho(\underline{r}) \phi_o(r - \underline{r}') d^3r' \qquad (1)$$

where ϕ is the scalar field constructed from the data, and ϕ_o is the point response function. As presented in a previous paper,[1] complete 3-D reconstructions can be achieved through deconvolution followed by iterations, or through matrix inversion. In this paper we formulate the propagation of errors in each of these two approaches and develop the methods to stabilize their performance in the presence of noise.

Usually, 3-D imaging devices have an axis of rotation (Fig. 2), which we shall take to be the z-axis. Due to the symmetry of the x and y axes, we shall write out only the x-axis explicitly and suppress the y-axis in most of the mathematical treatment and figures in order to facilitate presentation.

Deconvolution with Iterations

The deconvolution method[2,3] Fourier transforms Equation (1) to the frequency space (k-space) and solves for $R(\underline{k})$, the Fourier components of $\rho(\underline{r})$:

$$R(\underline{k}) = \begin{cases} \Phi(\underline{k})/\Phi_o(\underline{k}), & \text{if } \Phi_o(\underline{k}) \neq 0 \\ \text{undetermined}, & \text{if } \Phi_o(\underline{k}) = 0 \end{cases} \qquad (2)$$

where $\Phi_o(\underline{k})$, $\Phi(\underline{k})$ are the Fourier transforms of the point response function $\phi_o(\underline{r})$ and the data scalar field $\phi(\underline{r})$,[2] respectively. Some typical shapes of $\phi_o(\underline{r})$ and $\Phi_o(\underline{k})$ for positron cameras are given in Figs. 3 and 4. Hereafter, we shall refer to the region where $\Phi_o(\underline{k}) \neq 0$ as the "allowed cone," and that where $\Phi_o(\underline{k}) = 0$ as the "missing cone," respectively.

If noise $\Delta\Phi(\underline{k})$ is present in the data, the propagated error $E_d(\underline{k})$ in the reconstruction will be given by

$$E_d(\underline{k}) = \frac{\Delta\Phi(\underline{k})}{\Phi_o(\underline{k})}, \qquad \Phi_o(\underline{k}) \neq 0 \qquad (3)$$

Equation (3) shows that the error in the data is multiplied by the factor $1/\Phi_o(\underline{k})$ in deconvolution. In the region where $\Phi_o(\underline{k})$ is very small, the error will be greatly magnified. This is the case in the missing cone, as well as in the large $|k_x|$ region, since the result in [1] shows that for fixed $|k_z/k_x|$, $\Phi_o(\underline{k}) \propto 1/|k_x|$.

In the iterative scheme to be analysed below, $R(\underline{k})$ is set to zero in the missing cone. This procedure removes the instabilities there. A way to deal with the instabilities in the large $|k_x|$ region has been described in [2] in which the treatment of noise by Phillips[4] was recast. By imposing the smoothness condition

$$\int (\nabla^2 \rho(\underline{r}))^2 d^3r = \text{minimum}$$

on the solution $\rho(\underline{r})$ with the constraint that the total error in the data $\phi(\underline{r})$ is a constant, Equation (2) is modified to

$$R(\underline{k}) = \frac{\Phi(\underline{k})}{\Phi_o(\underline{k}) + \frac{\gamma(2\pi)^4 k^4}{\Phi_o(\underline{k})}} \qquad (4)$$

Here, $\gamma(>0)$ is an adjustable parameter which depends on the noise level. In the case of no noise, $\gamma = 0$, and Equation (4) reduces back to (2).

The modification made in Equation (4) can be viewed as the action of a low spatial frequency pass filter. The additional term in Equation (4)

$$\frac{\gamma(2\pi)^4 k^4}{\Phi_o(\underline{k})}$$

is negligible in low frequency compared to $\Phi_o(\underline{k})$, but increases rapidly in magnitude with frequency as both k^4 increases and $\Phi_o(\underline{k})$ decreases. Thus the information at low frequency is undistorted, whereas the noise at high frequency is suppressed.

A convenient way for specifying γ is to note the surface $S_{1/2}$ in k-space where the two terms in the denominator of Equation (4) become equal. At these frequencies the original Fourier components of the object are attenuated by a factor of 1/2. The surface $S_{1/2}$ should be chosen not too close to the origin so that reconstructions are not oversmoothed beyond the desirable resolution. As shown in [1,5], one way to recover the components in the missing cone is by means of the iterative scheme shown in Fig. 5. A qualitative proof of the convergence of this scheme has been given in [1,5]. In this paper we will give a more quantitative analysis. In actual reconstruction, we will be dealing with frequency components below a certain maximum frequency determined by such factors as the spatial resolution of the imaging system, the available computer core memory, etc. In Fig. 6 R_a represents the region in frequency space where $\Phi_o(\underline{k})$ is known, and R_b is the extent of the object. Define the operators A and B operating on function f defined in frequency space as follows:

$$Af = \chi_A f$$

$$Bf = F^{-1} \chi_B F f$$

where F and F^{-1} represent Fourier transformation and its inverse, and χ_A, χ_B are, respectively, the characteristic functions of R_a and R_b, defined as:

$$\chi_A(\underline{k}) = \begin{cases} 1 & \underline{k} \in R_a \\ 0 & \underline{k} \notin R_a \end{cases}$$

$$\chi_B(\underline{x}) = \begin{cases} 1 & \underline{x} \in R_b \\ 0 & \underline{x} \notin R_b \end{cases}$$

With these operators we can formulate the iteration procedure as follows. If $R(\underline{k})$ represents the Fourier spectrum of the object $\rho(\underline{r})$, and $S^{(0)}(\underline{k})$ the Fourier spectrum of $\rho(\underline{r})$ obtained from deconvolution, then

$$S^{(0)}(\underline{k}) = AR(\underline{k})$$

Fourier transforming $S^{(0)}(\underline{k})$ to the object space, setting the values outside the known extent of the object to zero, then inverse transforming to the frequency space, we get the first iterated spectrum $R^{(1)}(\underline{k})$:

$$R^{(1)}(\underline{k}) = BS^{(0)}(\underline{k}) = BAR(\underline{k})$$

Resetting the components of $R^{(1)}(\underline{k})$ inside the allowed cone to the original values given by $S^{(0)}(\underline{k})$ we get $S^{(1)}(\underline{k})$:

$$\begin{aligned} S^{(1)}(\underline{k}) &= S^{(0)}(\underline{k}) + (I - A)R^{(1)}(\underline{k}) \\ &= AR(\underline{k}) + (I - A)R^{(1)}(\underline{k}) \end{aligned}$$

Iterating we obtain the spectra $R^{(2)}(\underline{k})$, $S^{(2)}(\underline{k})$-----, $R^{(n)}(\underline{k})$,

$$\begin{aligned} R^{(2)}(\underline{k}) &= BS^{(1)}(\underline{k}) \\ S^{(2)}(\underline{k}) &= AR(\underline{k}) + (I - A)R^{(2)}(\underline{k}) \\ &\vdots \\ S^{(n-1)}(\underline{k}) &= AR(\underline{k}) + (I - A)R^{(n-1)}(\underline{k}) \\ R^{(n)}(\underline{k}) &= BS^{(n-1)}(\underline{k}) \\ &= BAR(\underline{k}) + (I - BA)R^{(n-1)}(\underline{k}) \end{aligned} \tag{5}$$

Subtracting $R(\underline{k})$ from both sides of Equation (5)

$$\begin{aligned} R^{(n)}(\underline{k}) - R(\underline{k}) &= BAR(\underline{k}) - R(\underline{k}) + (I - BA)R^{(n-1)}(\underline{k}) \\ &= (I - BA)(R^{(n-1)}(\underline{k}) - R(\underline{k})) \\ &\vdots \\ &= (I - BA)^{n-1}(R^{(1)}(\underline{k}) - R(\underline{k})) \\ &= (I - BA)^n(R^{(0)}(\underline{k}) - R(\underline{k})), \end{aligned}$$

where we now define $R^{(0)}(\underline{k}) = 0$. Thus we have

$$R^{(n)}(\underline{k}) = R(\underline{k}) - (I - BA)^n R(\underline{k}) \tag{6}$$

Note that throughout the iterations, all the spectra $R^{(i)}(\underline{k})$ operated on by BA satisfy

$$BR^{(i)}(\underline{k}) = R^{(i)}(\underline{k}) \tag{7}$$

In the Appendix it is shown that the operator BA operating on the functions satisfying Equation (7) is a positive definite operator. Thus the set of eigenfunctions $\{\psi_i\}$ of BA forms a complete set of functions which are orthonormal in the entire k-space, and orthogonal in the region R_a,[6]

$$\int_{\text{k-space}} \psi_i(\underline{k})\psi_j^*(\underline{k})d^3k = \delta_{ij}$$

$$\int_{R_a} \psi_j(\underline{k})\psi_j^*(\underline{k})d^3k = \lambda_i \delta_{ij}$$

Thus any function f in k-space which satisfies (7), ie. $Bf = f$, can be expanded into a series of ψ_i which represents f everywhere. If $Bf \neq f$, the expansion is still valid in the region R_a, but it does not necessarily represent f outside R_a. All the eigenvalues of BA lie between 0 and 1, ie. $0 < \lambda_i < 1$.

Decompose $R(\underline{k})$ into a linear combination of ψ_i

$$R(\underline{k}) = \sum_{i=0}^{\infty} a_i \psi_i(\underline{k})$$

Then Equation (6) becomes

$$R^{(n)}(\underline{k}) = \sum_{i=0}^{\infty} a_i(1 - (1-\lambda_i)^n)\psi_i(\underline{k})$$

The truncation error in terminating the iteration after n steps is thus given by

$$\begin{aligned} E_t^{(n)}(\underline{k}) &= R^{(n)}(\underline{k}) - R(\underline{k}) \\ &= -\sum_{i=0}^{\infty} a_i(1 - \lambda_i)^n \psi_i(\underline{k}) \end{aligned} \tag{8}$$

which is identical to that obtained by Papoulis[7] for the case of one-dimensional signals. This error tends to zero as $n \to \infty$.

The rate of convergence, ie. the rate $E_t^{(n)}(\underline{k})$ goes to zero, depends on the distribution of $\{\lambda_i\}$ and $\{a_i\}$. The distribution of $\{\lambda_i\}$ is determined by the regions R_a and R_b. In general the region R_b, which represents the extent occupied by the object, is fixed, whereas the region R_a can be changed by varying the angle subtended by the imaging device.

Fig. 7 shows a plot of the eignevalues for different opening angles of R_a, while R_b is chosen to be a 9 x 9 square sub-lattice in a 21 x 21 reconstruction lattice. It can be seen that the spectrum shifts towards zero as the angle decreases. The implication is that the convergence as expressed by Equation (8) will become worse when the angle of R_a is reduced.

To show this effect we apply the iterative algorithm to restore the missing cone components for a 2-D phantom. The reconstruction area is a 128 x 32 lattice, with equal lattice spacings in the x(i) and z(k) directions. The phantom has a square boundary with perpendicular diagonals which are both 11 lattice spacings long in the x and z directions, respectively. The Fourier components of the phantom outside the allowed cone were first set to zero, and then the iterative scheme was employed to recover them. The solid curve in Fig. 8 shows the root mean square error σ of the results after 20 iterations as a function of the opening angle of R_a. Here σ is defined as

$$\sigma = \sqrt{\frac{\sum_{i,j,k} (\text{reconstruction } (i,j,k) - \text{phantom}(i,j,k))^2}{\text{number of pixels}}}$$

Fig. 9 shows the corresponding results for a 3-D phantom. The shape of the point response function ϕ_o was in the form of a square pyramid with semi-vertical angle θ_o (Fig. 4). These two results show clearly the dependence of the truncation error $E_t^{(n)}(\underline{k})$ on the size of the opening angle of the allowed cone.

The above results can be viewed as reconstructions from perfect data generated by the phantoms, using deconvolution + iterations. For comparison, deconvolution + iterations were performed on a number of sets of finite statistical positron annihilation events

generated by the 2-D phantom. The values of σ for these results are plotted as the broken curves in Fig. 8. It can be seen that the truncation error is the main source of error at small angles of R_a, whereas the statistical error dominates at large angles. The minimum in σ which occurs for finite statistical reconstructions is due to the competition of two effects: the improvement in the behavior of the eigenvalues $\{\lambda_i\}$ on the one hand, and the increase in the error magnitude of $\phi(\underline{r})$ on the other, as the angle increases while keeping the number of the annihilation events fixed.

Figs. 8 and 9 give only the relative magnitude of the truncation error in iterating as a function of the angular size of the allowed cone. To get a qualitative feeling of how well the iterations work at small allowed-cone angles,we applied the algorithm to restore the missing cone components for a two-dimensional point source located inside the square boundary of the 2-D phantom of Fig. 8. The assumed allowed cone subtends a semi-vertical angle of $\tan^{-1}(0.5)$ along the k_x-axis. The constraint that the object is non-negative was also utilized in the iterations.

Fig. 10A shows the shape of the point source at the center of the square with the Fourier components in the missing cone set to zero. Only the middle 32 x 32 picture elements are shown. Two kinds of distortions are seen. Firstly, the point source is considerably widened. Secondly, decaying oscillating ridges appear on the edges of the detection cone corresponding to the assumed missing cone and centered at the point source.

Fig. 10B shows the same point source after 30 iterations. The ridges are lowered in height. Also, the point source is significantly narrowed.

Fig. 11 illustrates the corresponding results for a point source located on the boundary of the square: in this case at the corner with the lowest k-index. The improvement after iterations is much more impressive in this case than that with the point source at the center of the square. The improvement is due to the fact that for the point source on the boundary, at least two of the four decaying ridges lie outside the square and thus are repeatedly reset to zero in iterating; whereas for the point source at the center, only those low-amplitude lobes of the ridges far away from the point source are reset to zero, producing smaller effect in restoring the missing cone components in comparison.

These results indicate that the volume elements on the boundary of the phantom will reconstruct better through iterations than the interior volume elements.

Besides the truncation error $E_t^{(n)}$, the measured error $\Delta S(\underline{k})$ in the frequency components in the allowed cone R_a also propagates in the iterations. Following Papoulis,[7] we expand $\Delta S(\underline{k})$ into a series of eigenfunctions of BA in the region R_a

$$\Delta S(\underline{k}) = \sum_{i=0}^{\infty} c_i \psi_i(\underline{k}) \qquad k \in R_a$$

$$\text{with } |\Delta S|^2 = \int_{R_a} |\Delta S(\underline{k})|^2 d^3k = \sum_i c_i^2 \lambda_i$$

Since the iteration is a linear process, the result after n steps of iterations on the measured frequency components, $S(\underline{k}) + \Delta S(\underline{k})$, is given by $R^{(n)}(\underline{k}) + \Delta R^{(n)}(\underline{k})$ where

$$\Delta R^{(n)}(\underline{k}) = \sum_{i=0}^{\infty} c_i (1 - (1-\lambda_i)^n) \psi_i(\underline{k})$$

An upper bound of the magnitude of the propagated error $\Delta R^{(n)}(\underline{k})$ can be estimated as follows:

$$|\Delta R^{(n)}|^2 = \sum_i c_i^2 (1 - (1-\lambda_i)^n)^2$$

$$= \sum_i c_i^2 \lambda_i^2 [1 + (1-\lambda_i) + \ldots + (1-\lambda_i)^{n-1}]$$

Since all the λ_i's lie in (0,1), we have

$$1 + (1-\lambda_i) + \ldots + (1-\lambda_i)^{n-1} < n$$

Thus

$$|\Delta R^{(n)}|^2 < n^2 \sum_{i=0}^{\infty} c_i^2 \lambda_i = n^2 |\Delta S|^2$$

Therefore

$$|\Delta R^{(n)}| < n |\Delta S| \ .$$

Matrix Inversion

The matrix method[8] Fourier transforms Equation (1) in the x dimension only and solves the resulting integral equation in the z dimension for every spatial frequency k_x,

$$\varphi(k_x,z) = \int_{z_1}^{z_2} \varphi_o(k_x, z-z') p(k_x,z') dz' \qquad (9)$$

where φ, φ_o and p are the partial Fourier transforms of ϕ, ϕ_o and ρ in the x dimension. In [1], it has been shown that for $k_x \neq 0$ a unique solution exists which is given by

$$p(k_x,z) = \sum_i \frac{(g_i^*, \varphi)}{\alpha_i} g_i(k_x,z)$$

where α_i, g_i are the eigenvalues and eigenfunctions of the integral operator (9), and

$$(g_i^*, \varphi) = \int_{-\infty}^{\infty} g_i^*(k_x,z) \varphi(k_x,z) dz$$

If the data $\varphi(k_x,z)$ contain error $\Delta\varphi(k_x,z)$, then the propagated error in inversion will be

$$E_m(k_x,z) = \sum_i \frac{(g_i^*, \Delta\varphi)}{\alpha_i} g_i(k_x,z) \qquad (10)$$

Again, the expression (10) shows that the major errors in the reconstruction come from the small eigenvalues.

As shown in [1], φ_o is of the form

$$\varphi_o(k_x,z-z') = \int_{-\theta_o}^{\theta_o} \frac{F(\theta)}{\pi} \exp[2\pi i k_x \tan\theta (z-z')] d\theta$$

where $F(\theta)$ is an angular weighting factor which is positive inside the detection cone and vanishes outside. For the particular case $F(\theta) = \cos^{-2}\theta$ inside the detection cone, the expression for φ_o simplifies to

$$\varphi_o(k_x,z-z') = \frac{1}{\pi} \int_{-\theta_o}^{\theta_o} \exp[2\pi i k_x \tan\theta (z-z')] d(\tan\theta)$$

$$= \frac{\sin[2\pi k_x \tan\theta_o (z-z')]}{\pi^2 k_x (z-z')}$$

The eigenvalue equation of this kernel is

$$\lambda_i g_i(k_x,z) = \int_{z_1}^{z_2} g_i(z) \frac{\sin 2\pi k_x \tan\theta_o (z-z')}{\pi^2 k_x (z-z')} dz' \qquad (11)$$

On rearranging, Equation (11) becomes

$$(\pi k_x \lambda_i) g_i(k_x,z) = \int_{z_1}^{z_2} \frac{\sin(2\pi k_x \tan\theta_o (z-z'))}{\pi(z-z')} g_i(k_x,z')dz'$$

which is the zeroth order prolate spheriodal eigenvalue equation. Thus $\{\pi k_x \lambda_i\}$ is a set of zeroth order prolate spheroidal eigenvalues. As pointed out by Slepian and Pollak,[9] the distribution of these eigenvalues depends on the quantity $c = 2\pi k_x \tan\theta_o (z_2-z_1)$, and for a fixed c, the eigenvalues fall off to zero rapidly with increasing i once i exceeds $(2/\pi)c$. These eigenvalues are shown in Fig. 12. This means that noise multiplication would be especially serious whenever k_x, $\tan\theta_o$, or (z_2-z_1) becomes small.

One way to stabilize the method, for fixed $\tan\theta_o$ and (z_2-z_1), is to discard the results at small k_x where the errors dominate, and, by making use of the finite extent of the object in the x dimension, fill in those values using the results obtained from the higher k_x values through the iterative scheme shown in Fig. 13.

Another way to stabilize the matrix method is by means of the smoothing procedure proposed by Phillips[4] and Twomey.[10] Instead of solving the ill-conditioned matrix equation

$$Y = AX$$

which is the digital version of Equation (9), another matrix equation with a modified kernel

$$Y = (A + \gamma B)X$$

is solved. Here the matrix B is obtained from A in the following manner:

$$b_{1k} = a_{k-2,1} - 4a_{k-1,1} + 6a_{k,1} - 4a_{k+1,1} + a_{k+2,1}$$

and γ is a parameter dependent on the noise level in the data. This procedure will remove the instabilities at the high spatial frequencies k_z for each of the operators (9) characterized by k_x.

Comparison Between Deconvolution + Iterations and Matrix Inversion

After analyzing the basic properties of the deconvolution + iterations and the matrix methods, a comparison of their relative merit is now in order. If the data contain no error or only a negligible amount of error, the main error in the result of deconvolution + iterations will come from the truncation error $E_t^{(n)}$ in iterating, as the deconvolution error E_d will be insignificant in this case. For the matrix method, the inversion error E_m will also be negligible. The only unknown solution at $k_x = 0$ could be filled in by continuation from other non-zero k_x values, and the error introduced in continuing the solution to one point would be very small compared to the error $E_t^{(n)}$ in continuing the solution outside R_a for general opening angle $2\theta_o$. Thus in the case of very small amounts of noise, the matrix inversion has an advantage over the deconvolution + iterations approach, unless some accelerated scheme can be devised to reduce $E_t^{(n)}$.

To predict their relative performance in the presence of significant amounts of noise, it suffices to compare the condition numbers of the deconvolution operation and matrix inversion respectively. For deconvolution, the condition number κ_d is given by

$$\kappa_d = \frac{(\Phi_o(\underline{k}))_{max}}{(\Phi_o(\underline{k}))_{min}}$$

and for each $k_x \neq 0$, the condition number $\kappa_m(k_x)$ of the integral operator (9) is given by

$$\kappa_m(k_x) = \frac{\alpha_{max}}{\alpha_{min}}$$

Now Equation (A.2) in [1] shows that $\Phi_o(\underline{k})$ is in the form

$$\Phi_o(k_x,k_z) = \frac{F(\theta_i)\cos^2\theta_i}{\pi|k_x|}$$

where $\tan\theta_i = -k_z/k_x$, and $F(\theta)$ is the angular factor used in constructing $\phi_o(\underline{r})$ [1]. For each $k_x \neq 0$, the condition number is thus given by

$$\kappa_d(k_x) = \frac{(F(\theta)\cos^2\theta)_{max}}{(F(\theta)\cos^2\theta)_{min}}$$

In general the maximum and minimum values of $F(\theta)\cos^2\theta$ do not differ by several orders of magnitude; in fact, for the generally used angular factors $F(\theta) = 1$ and $F(\theta) = \cos^{-2}\theta$, $\kappa_d(k_x)$ equals $\sec^2\theta_o$ and 1 respectively. On the other hand, α_{max} and α_{min} can differ by a factor of order hundreds of thousands; in fact, α_{min} asymptotically approaches zero as the index of the eigenvalue increases. The decrease of α with the index is especially fast at small values of k_x and θ_o. Thus matrix inversion is expected to be more unstable to noise than deconvolution + iterations.

This comparison is still valid even if the iterative scheme Fig. 13 is employed to stabilize the matrix method. The reason is the following. In iterating, all the solutions from inversion with k_x below some $k_o (> 0)$ are discarded, and they are filled in using those with $k_x \geq k_o$. But as the solution from inversion for every k_x contains both reliable and unreliable components corresponding to the large and small eigenvalues of the integral operator (9) characterized by that k_x, the solutions used to start the iterations for the matrix method always contain some unreliable components. In comparison, the deconvolution results used to start iterations do not have such a mixed population of reliable and unreliable components.

Discrete Angular Input Data

Analytic continuation in limited-angle reconstruction is not restricted to continuous angular input data only. With slight modifications it can be applied to discrete angular input data from a device such as a limited-angle pinhole array.

Fig. 14 shows a limited-angle pinhole array imaging a two-dimensional object. The pinholes are separated from each other by a gap d, and each of them produces a fan beam projection of the object on a detector at a distance s away from the pinhole array. For simplicity the images from different pinholes are assumed to be non-overlapping. Through the coordinate transformation represented by

$$\bar{z} = \frac{s}{s+z} z \ , \quad \bar{x} = \frac{s}{s+z} x$$

the fan beam projection produced by each pinhole is deformed into a parallel beam projection of the distorted object $\bar{\rho}(\bar{x},\bar{z})$ which has a one-to-one correspondence with the original object $\rho(x,z)$ through the equation[11]:

$$\bar{\rho}(\bar{x},\bar{z})d\bar{x}d\bar{z} = (\frac{s}{s+z})^2 \rho(x,z)dxdz$$

By the projection theorem, each of these parallel projections, upon Fourier transformation, yields a line of the Fourier components of the object up to the maximum frequency k_{max} imposed by the resolution Δ of the detector, where $k_{max} = \frac{1}{2\Delta}$. This is illustrated in Fig. 15, which is again a limited-angle imaging problem, the angular range $2\theta_o$ being limited by the lateral extent l_{max} of the outermost pinhole

$$\theta_o = \tan^{-1}(\frac{l_{max}}{s})$$

The other missing components can be recovered from those shown in Fig. 15, through analytic continuation, if the resolution of the Fourier components in k_z and the extent L_z of the object in the z direction satisfy the Nyquist sampling condition.[12] Referring to Fig. 15, this condition can be expressed as

$$k_{max}\cos\theta_o|\tan\theta_i - \tan\theta_{i-1}| \leq \frac{1}{2L_z}$$

$$\text{or} \quad \frac{s}{\Delta\sqrt{s^2 + l_{max}^2}} \leq \frac{1}{L_z}$$

Conclusions

We have shown that the deconvolution + iterations algorithm is stable to noise, and that the matrix inversion algorithm can be stabilized by iterations or smoothing. The iterative scheme works will even in cases where the data inputs are restricted to a small continuous angular range. It was also found that complete reconstruction is possible in imaging situations involving discrete data inputs confined to limited angular range if the Nyquist sampling condition is satisfied.

Acknowledgements

We would like to take this opportunity to thank Dr. Alberto Grunbaum for many helpful discussions.

This work was supported by the Physics Division of the U. S. Department of Energy under Contract No. W-7405-ENG-48.

Appendix

Proof for the Positive Definiteness of BA

We want to prove that BA is a positive definite operator for all functions ψ satisfying $B\psi = \psi$.

Lemma 1 For all ψ such that $A\psi = \psi$, B is a positive definite operator.

Proof: $B\psi = 0$

$\Rightarrow F^{-1}(\chi_B F \chi_A \psi) = 0$

$\Rightarrow \chi_B F \chi_A \psi = 0$

$\Rightarrow F\chi_A\psi = 0$ ($\because F\chi_A\psi$ is an entire function)

$\Rightarrow \chi_A\psi = 0$

$\Rightarrow \psi = 0$

Lemma 2 For all ψ such that $B\psi = \psi$, A is a positive definite operator.

Proof: $A\psi = 0$

$\Rightarrow \chi_A F^{-1}\chi_B F\psi = 0$

$\Rightarrow F^{-1}\chi_B F\psi = 0$ ($\because F^{-1}\chi_B F\psi$ is an entire function)

$\Rightarrow \psi = 0$

Combining lemma 1 and lemma 2 we get the desired result.

References

[1] Tam, K. C., Perez-Mendez, V., and Macdonald, B., LBL-8539, submitted to Physics in Medicine and Biology.

[2] Chu, G., and Tam, K. C., Phys. Med., Biol., 22 (1977) 245.

[3] Tam, K. C., Chu, G., Perez-Mendez, V. and Lim, B. C., IEEE Trans. Nucl. Sci., NS-25 (1978) 152.

[4] Phillips, D. L., J. Ass. Comput. Mach., 9 (1962) 84.

[5] Tam, K. C., Perez-Mendez, V., and Macdonald, B., IEEE Trans. Nucl. Sci., NS-26 (1979) 2797.

[6] Slepian, D., Bell Syst. Tech. J., 43 (1964) 3009.

[7] Papoulis, A., IEEE Trans. Circuits Syst., CAS-22 (1975) 735.

[8] Chang, L. T., Macdonald, B., and Perez-Mendez, V., IEEE Trans. Nucl. Sci., NS-23 (1976) 568.

[9] Slepian, D., and Pollak, H. O., Bell Syst. Tech. J., 40 (1961) 43.

[10] Twomey, S., J. Ass. Comput. Mach., 10 (1963) 97.

[11] Chiu, M. Y., Barrett, H. H., Simpson, R. G., Chou, C., Arendt, J. W., and Gindi, G. R., Optical Sciences Center and Department of Radiology, University of Arizona, Tucson, Arizona report.

[12] Brigham, E. O., 1974, The Fast Fourier Transform (Englewood, New Jersey: Prentice-Hall) p. 85.

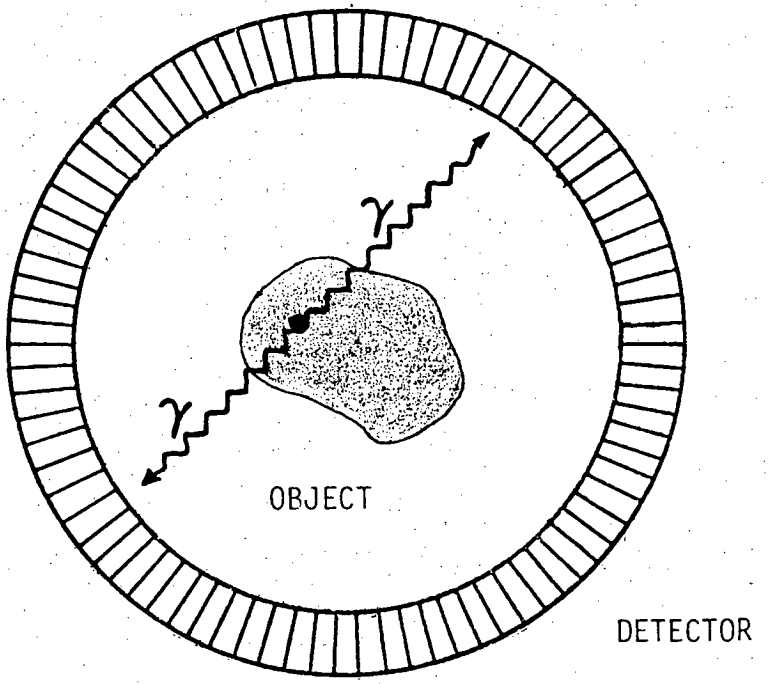

A. RING POSITRON CAMERA

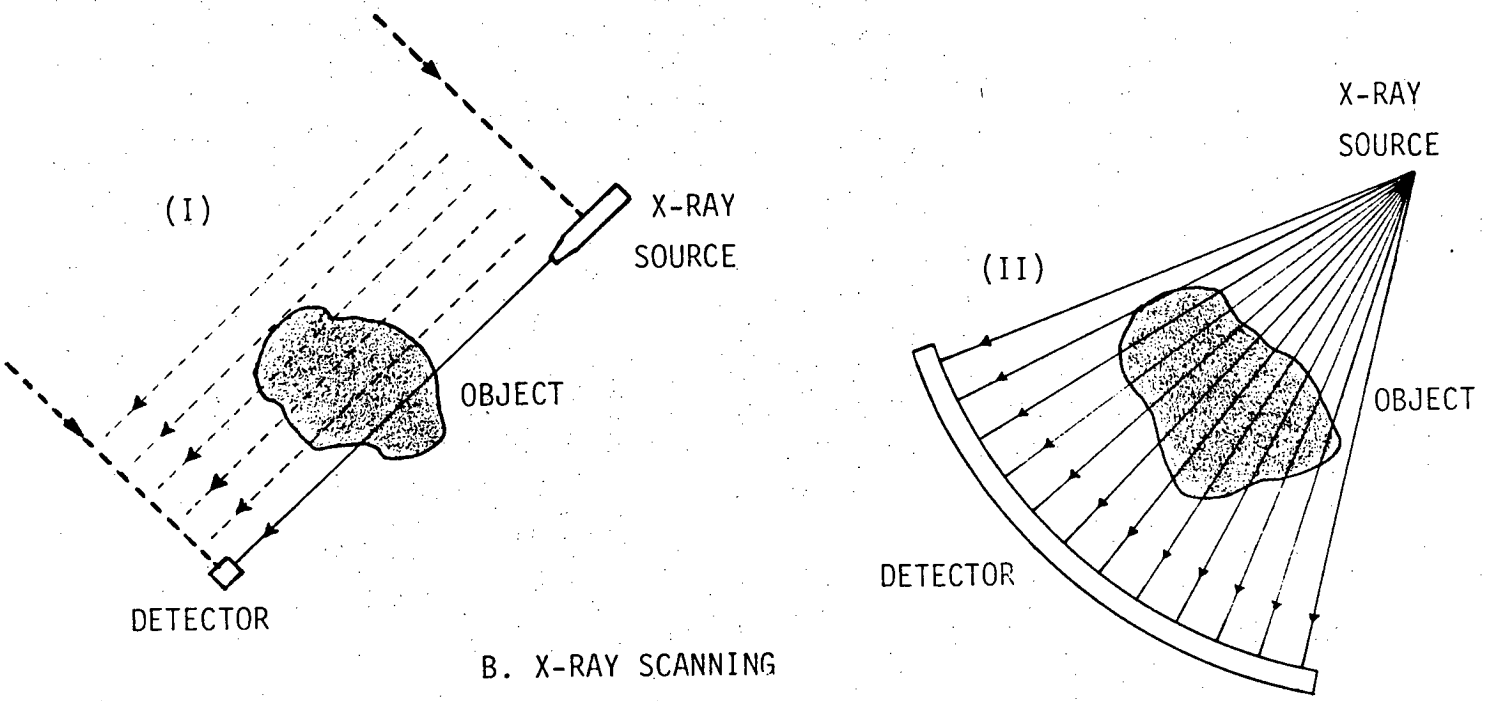

B. X-RAY SCANNING
(I) PARALLEL BEAM
(II) FAN BEAM

Fig. 1. 2-D imaging devices.

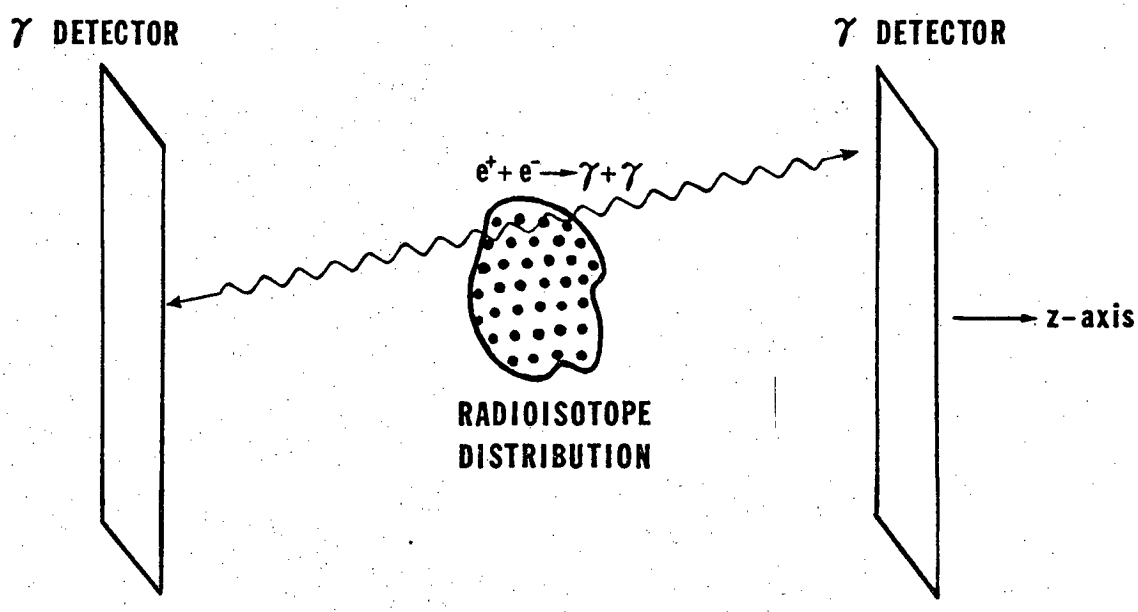

A. PLANAR POSITRON CAMERA

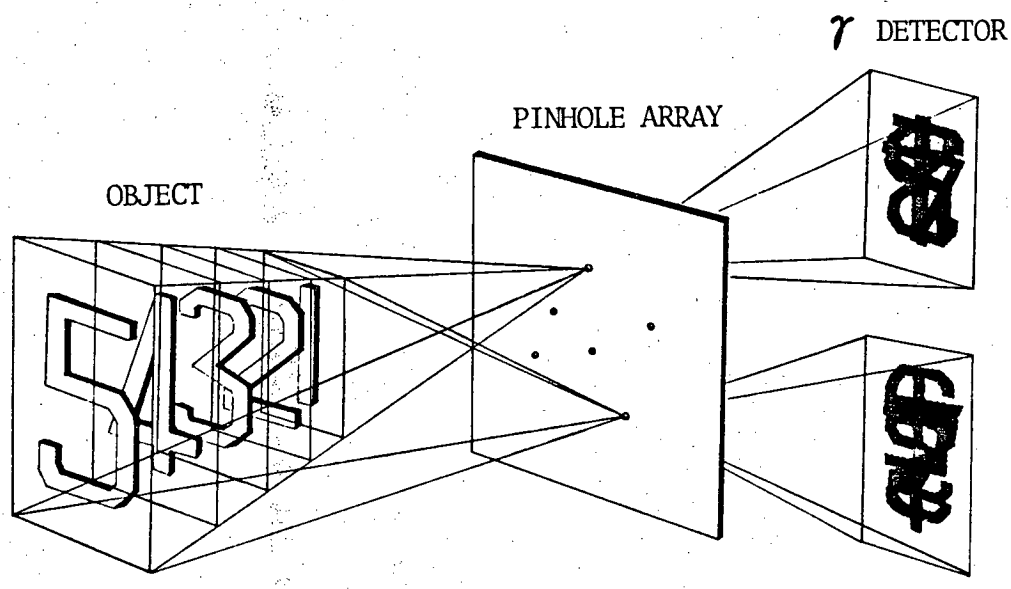

XBL 7812-13269

B. PINHOLE IMAGING DEVICE

Fig. 2. 3-D imaging devices.

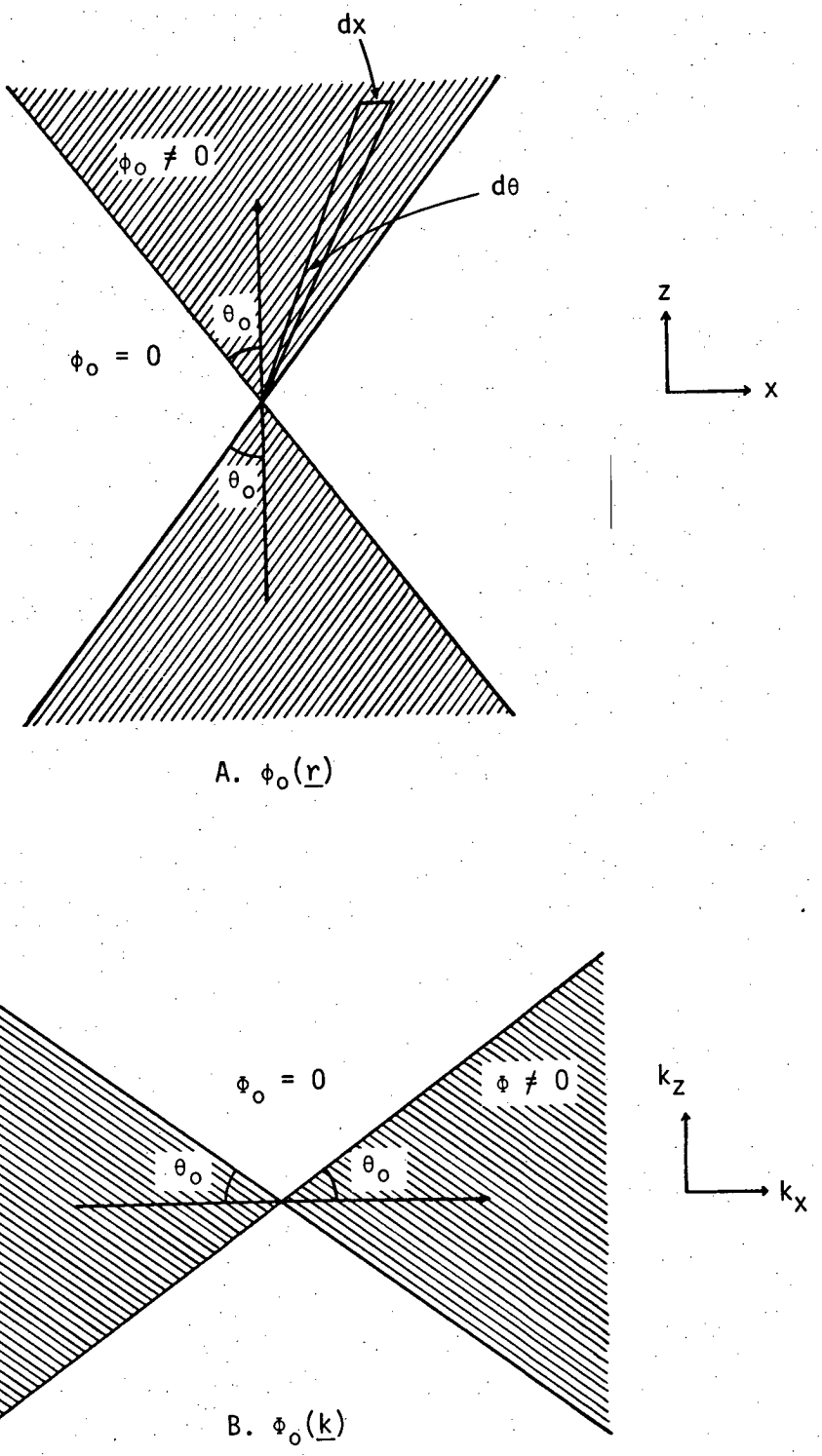

Fig. 3. A 2-D point response function $\phi_o(\underline{r})$ and its optical transfer function $\Phi_o(\underline{k})$.

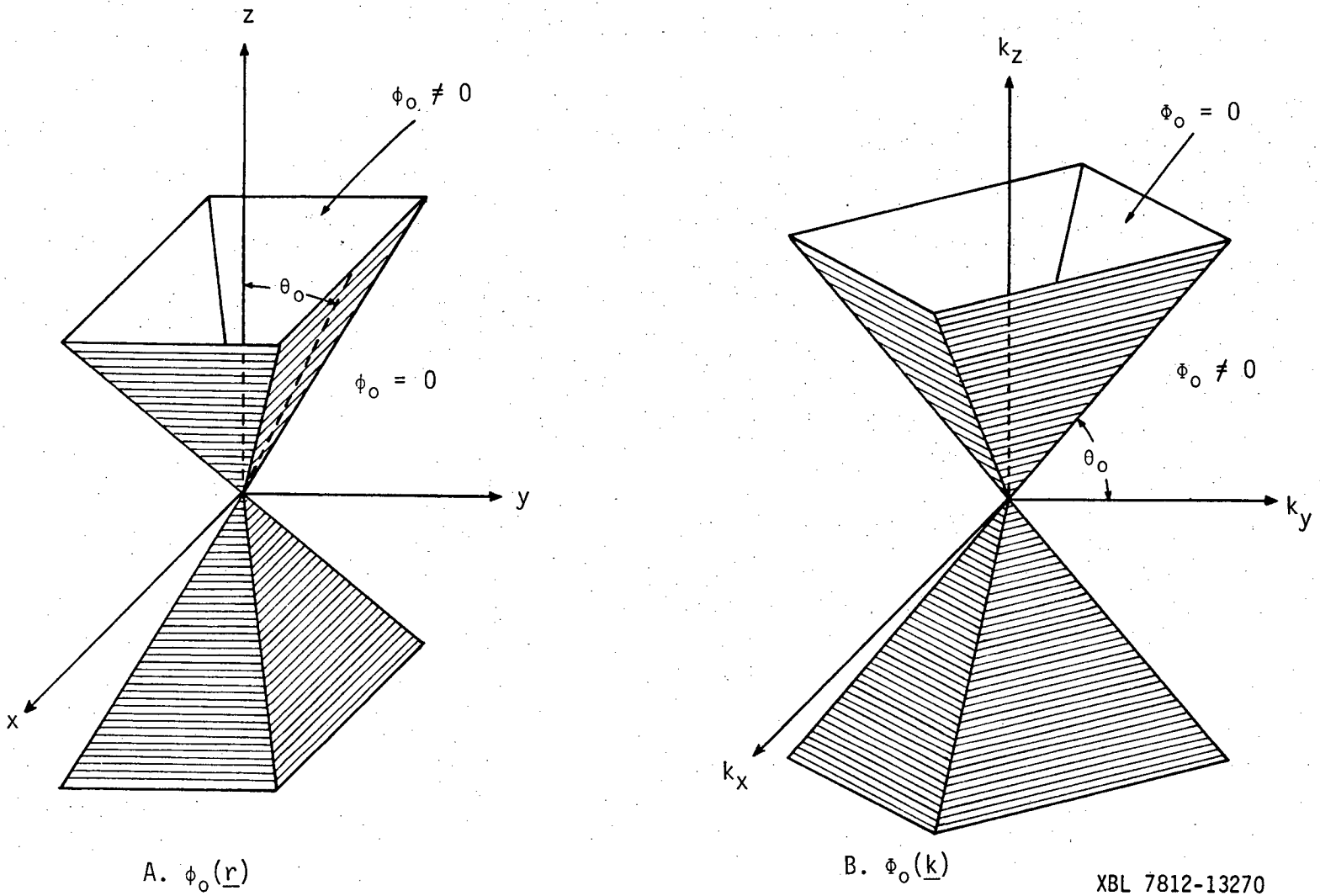

Fig. 4. A pyramidal 3-D point response function $\phi_o(\underline{r})$ and its optical transfer function $\Phi_o(\underline{k})$.

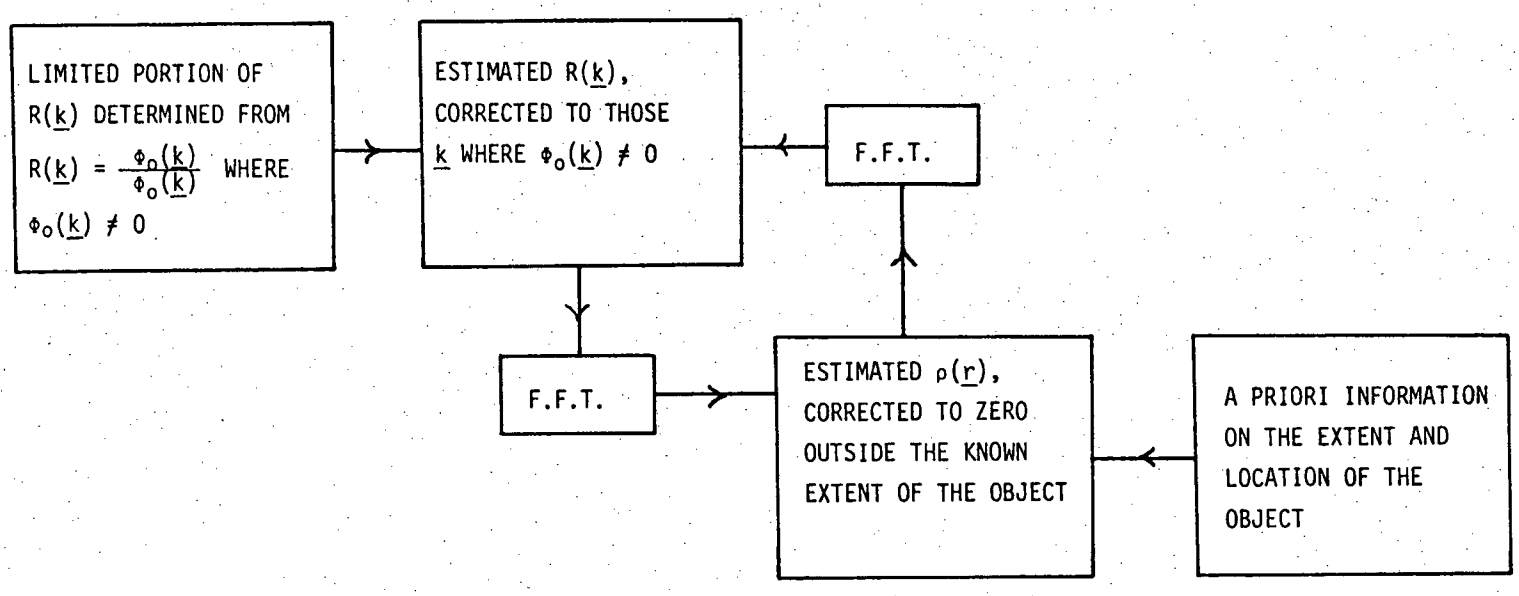

Fig. 5. Iterative scheme to extend the spectrum R(k) beyond the allowed cone.

XBL 796-10266

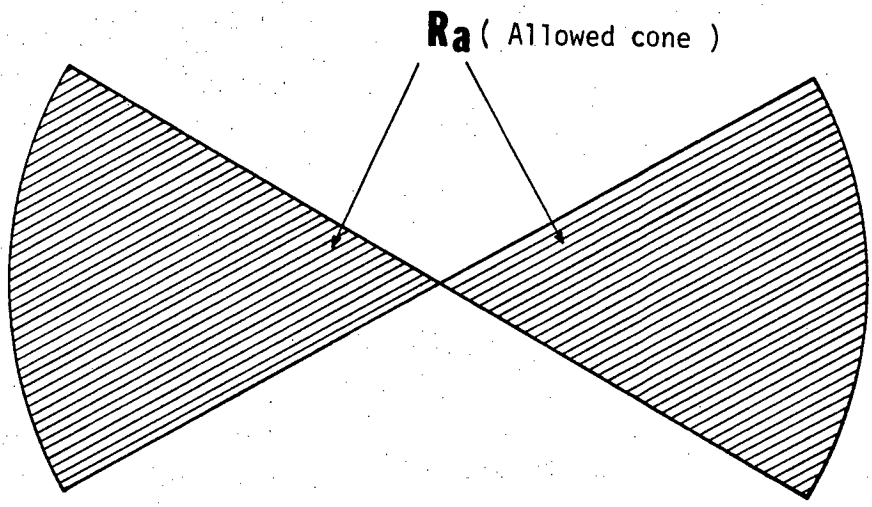

Frequency space ($\underline{k}$)

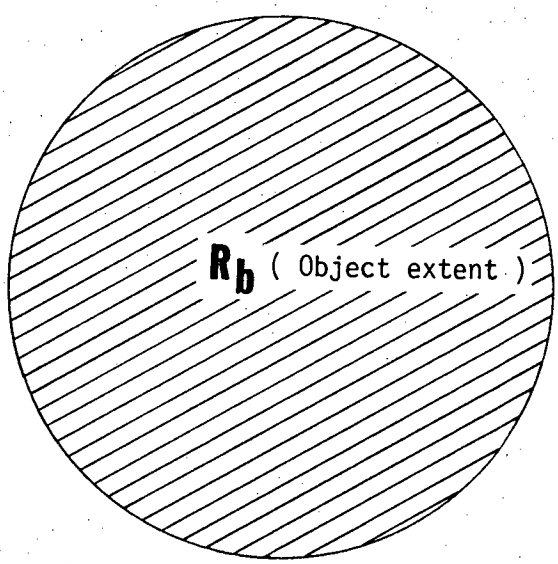

Object space ($\underline{r}$)

XBL 798-11176

Fig. 6. Schematic representations of the allowed cone and the object extent.

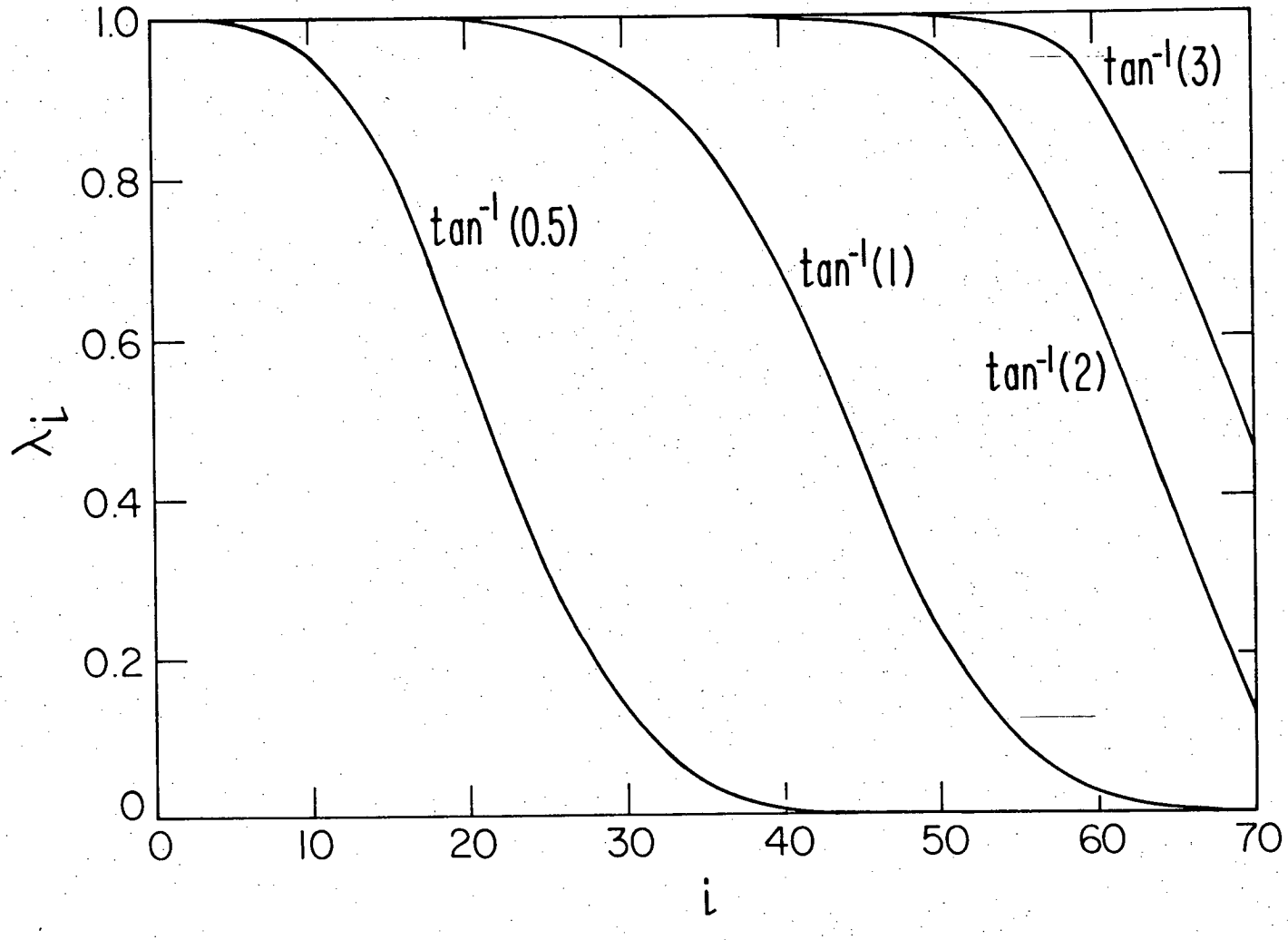

XBL 798-2379

Fig. 7. Eigenvalues of BA for a 2-D problem for various semi-vertical angles of the allowed cone.

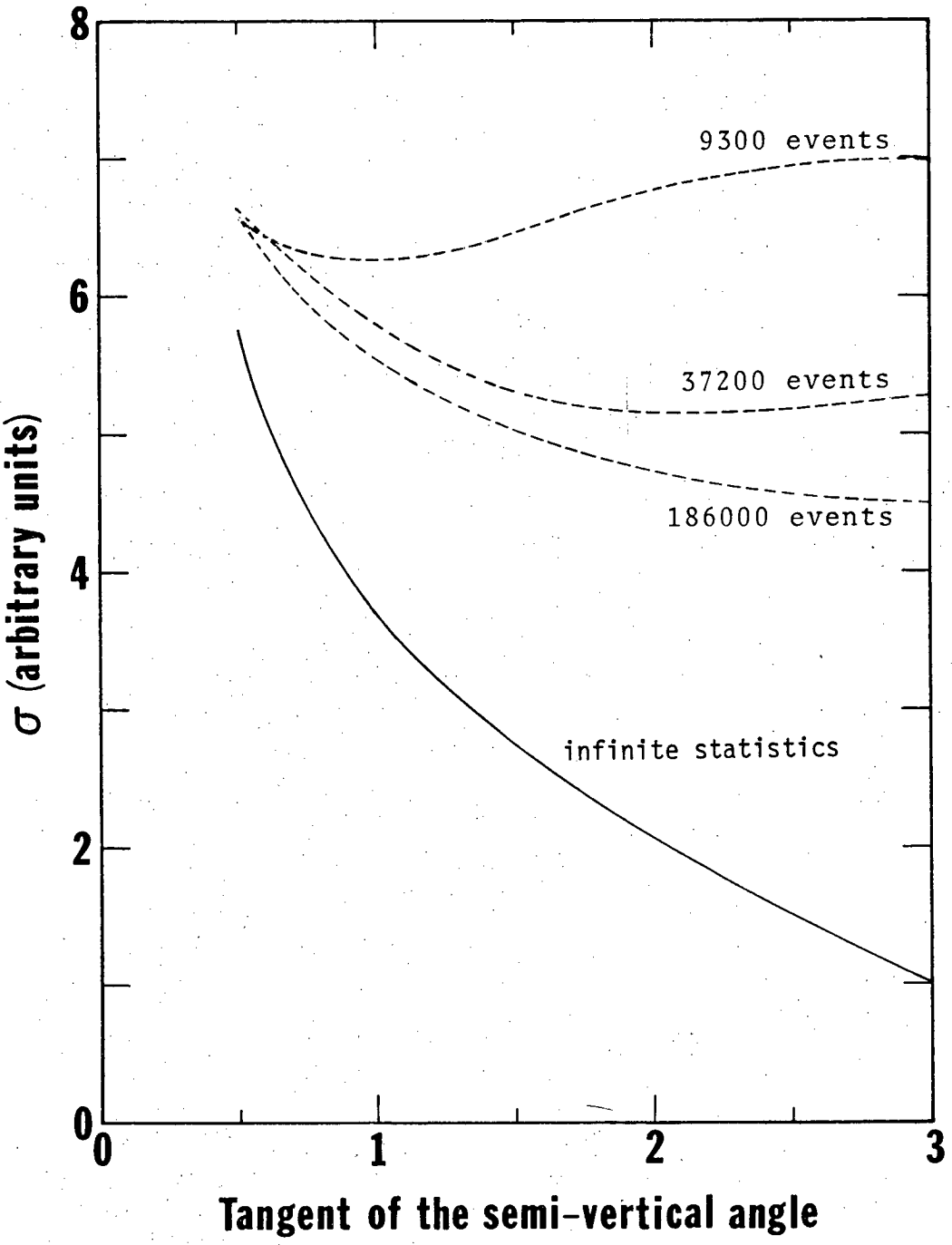

XBL 798-2378

Fig. 8. Root mean square error in reconstructing a 2-D phantom as a function of the semi-vertical angle of the allowed cone for various statistics.

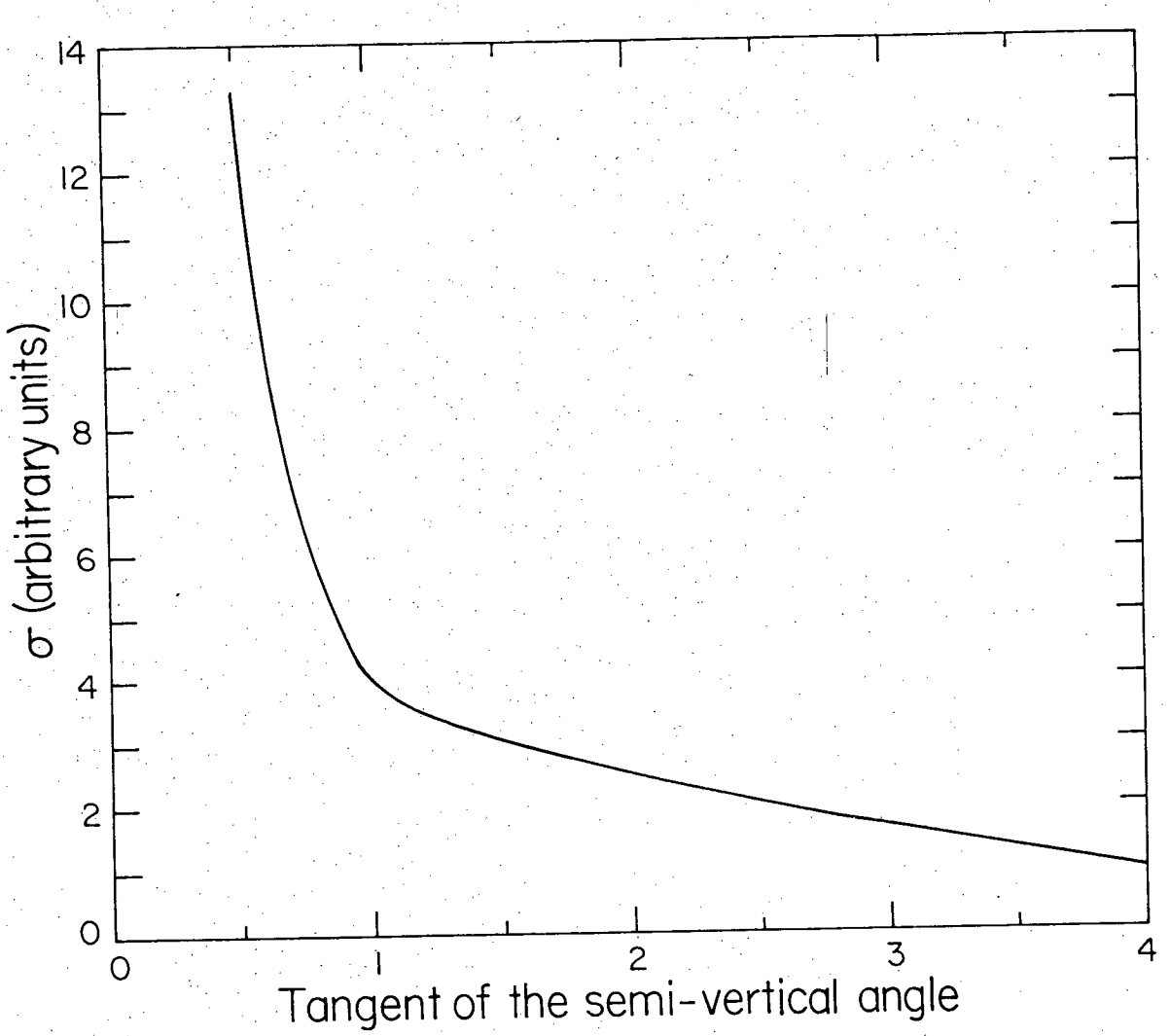

XBL 798-2380

Fig. 9. Root mean square error after 20 iterations as a function of the semi-vertical angle of the allowed cone for a 3-D phantom.

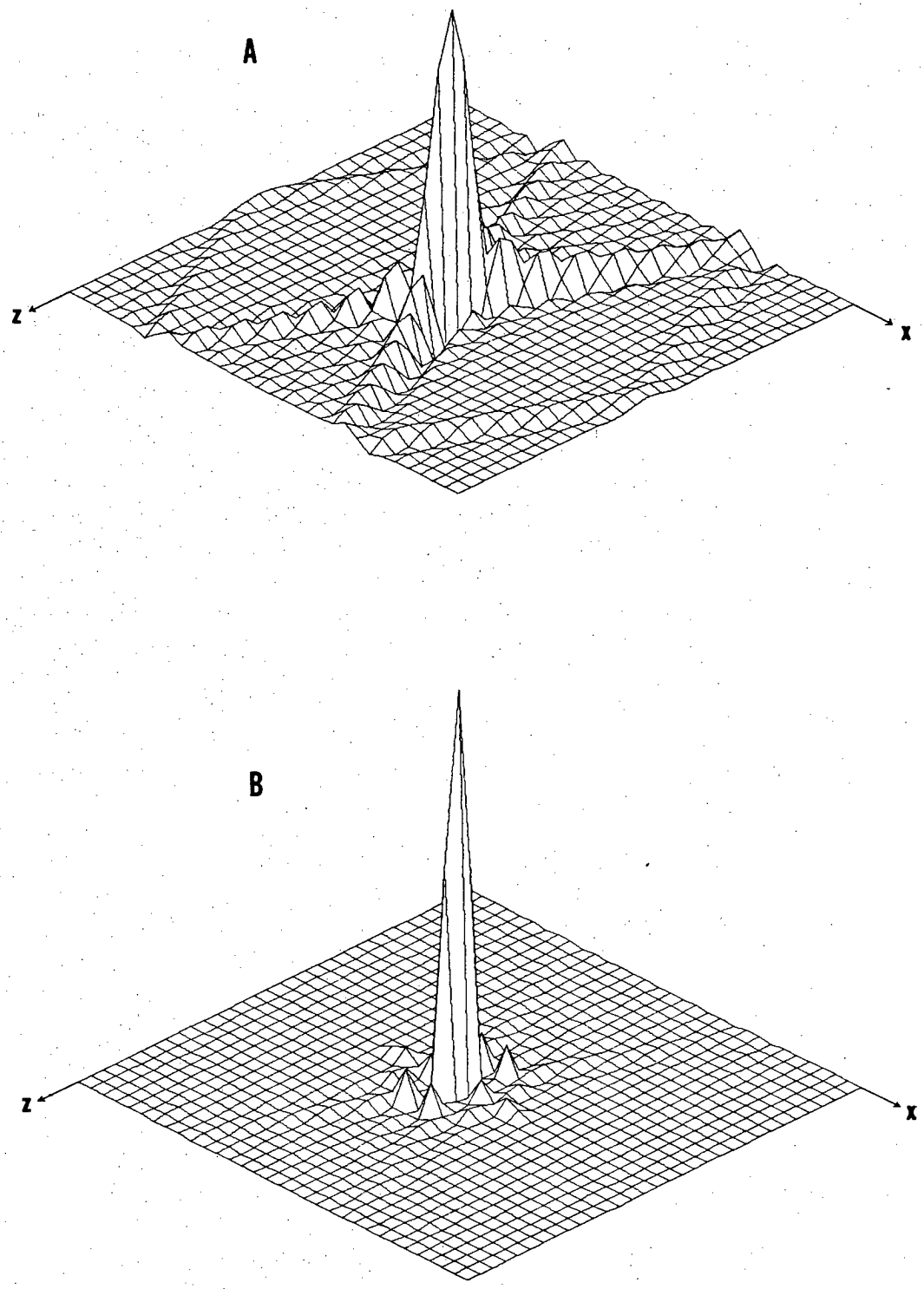

XBL 7910-12148

Fig. 10. Recovering the missing cone components for a 2-D point source located at the center of a square which acts as the finite object extent in the iterations. The semi-vertical angle of the allowed cone is $\tan^{-1}(0.5)$.

A. The point source with the missing cone components set to zero.

B. The point source after 30 iterations.

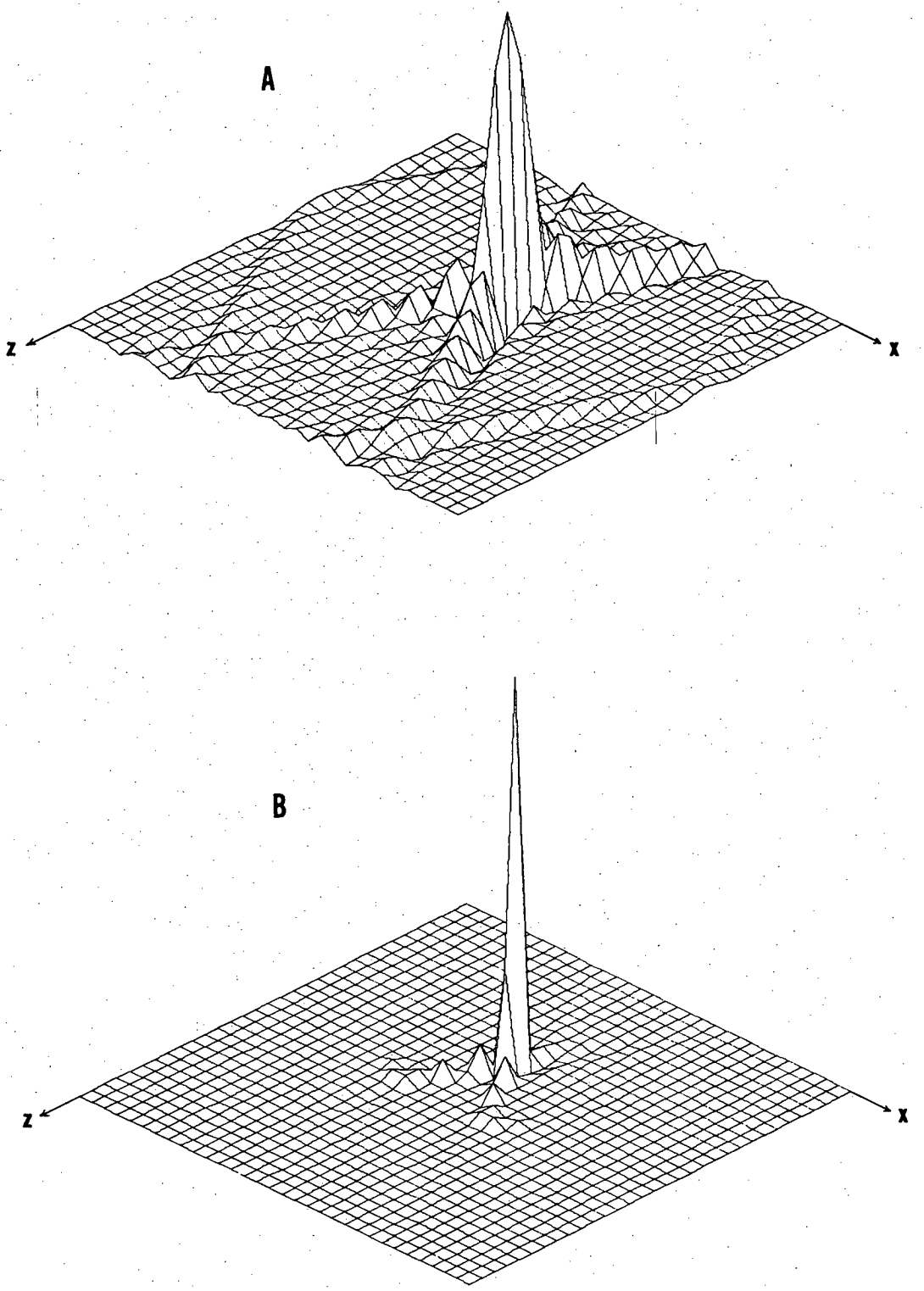

XBL 7910-12147

Fig. 11. Recovering the missing cone components for a 2-D point source located on the boundary of a square which acts as the finite object extent in the iterations. The semi-vertical angle of the allowed cone is $\tan^{-1}(0.5)$.

A. The point source with the missing cone components set to zero.

B. The point source after 30 iterations.

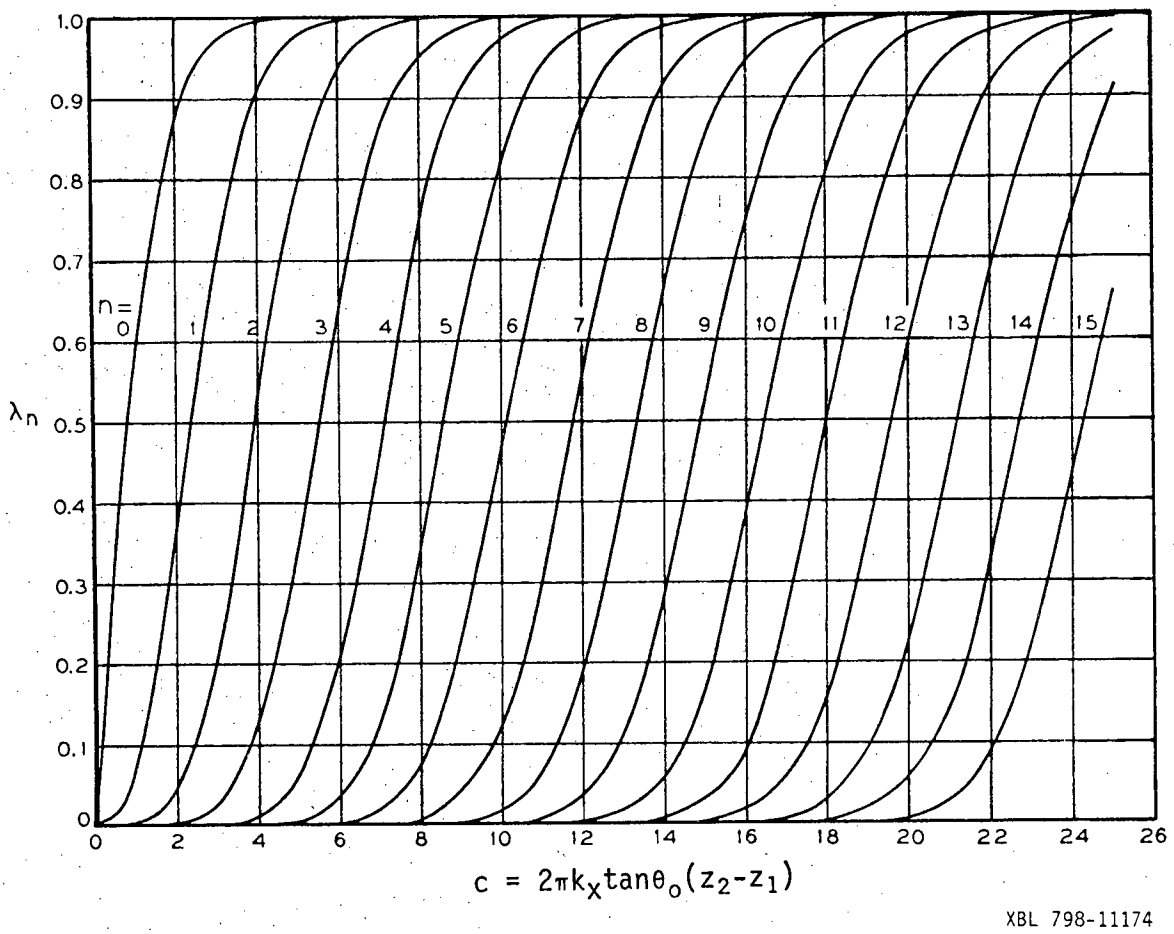

Fig. 12. Eigenvalues of the zeroth order prolate spheroidal equation.

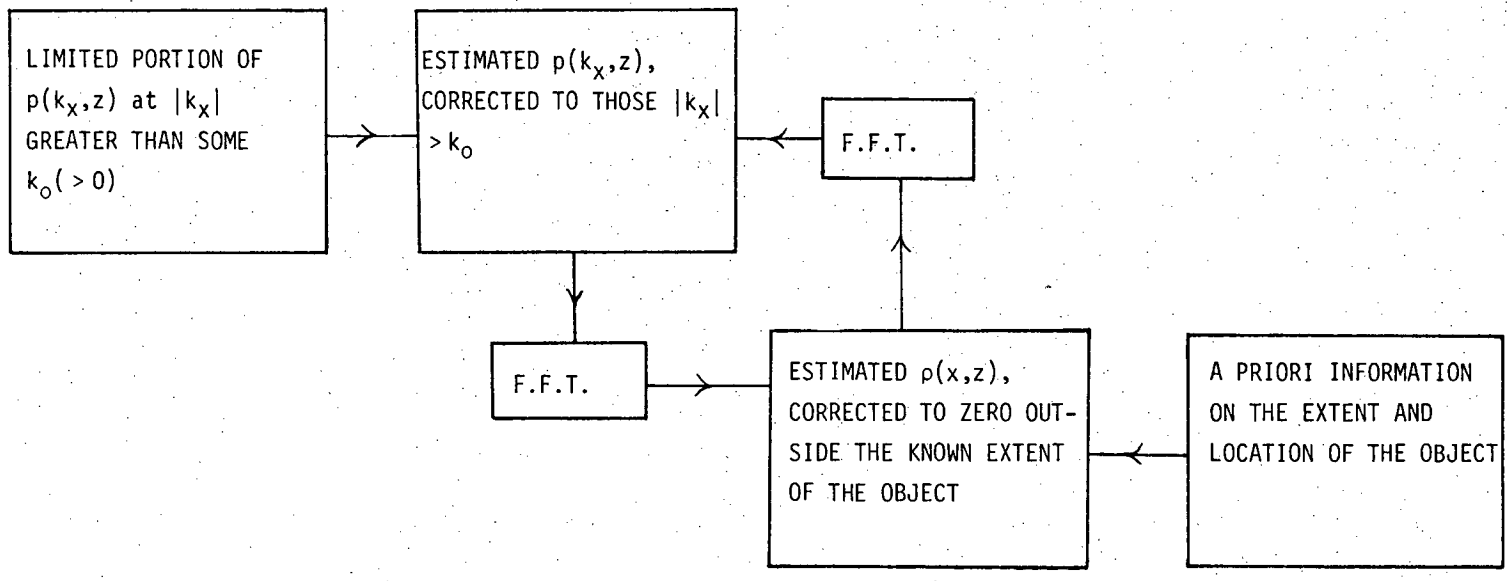

Fig. 13. Iterative scheme to stabilize the matrix inversion algorithm.

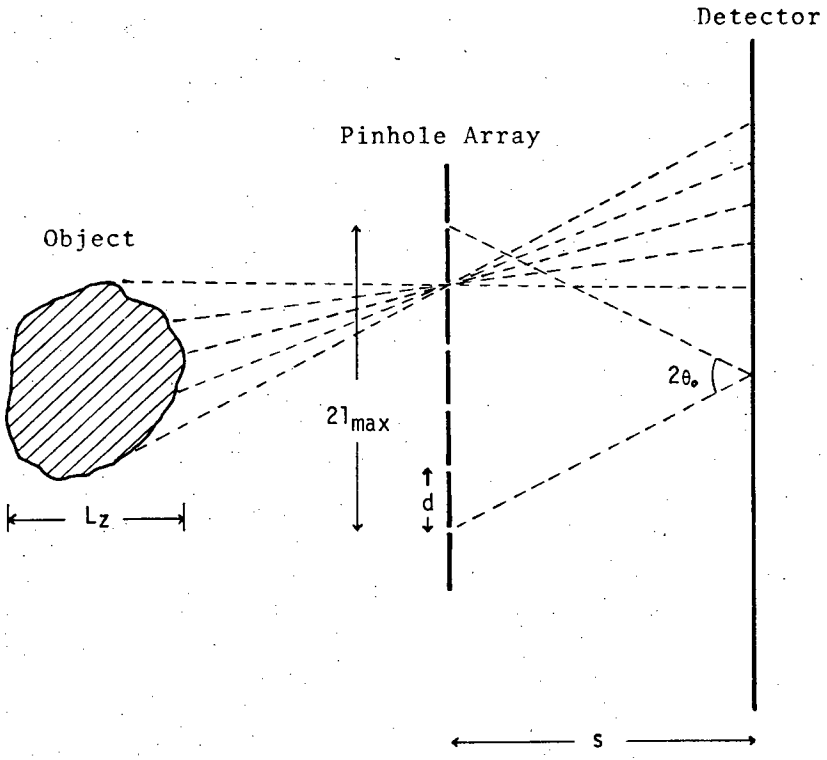

Fig. 14. Schematic figure of pinhole array.

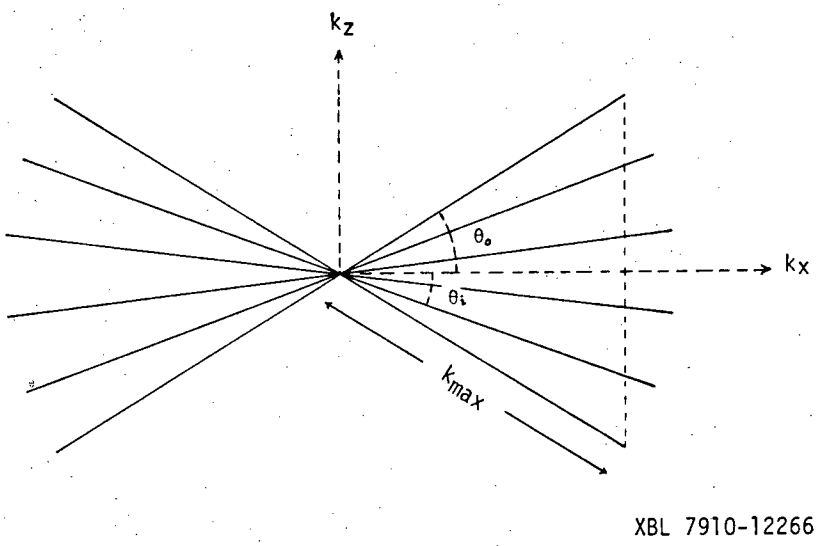

Fig. 15. Fourier components of the distorted object in pinhole array imaging.

This report was done with support from the Department of Energy. Any conclusions or opinions expressed in this report represent solely those of the author(s) and not necessarily those of The Regents of the University of California, the Lawrence Berkeley Laboratory or the Department of Energy.

Reference to a company or product name does not imply approval or recommendation of the product by the University of California or the U.S. Department of Energy to the exclusion of others that may be suitable.

TECHNICAL INFORMATION DEPARTMENT
LAWRENCE BERKELEY LABORATORY
UNIVERSITY OF CALIFORNIA
BERKELEY, CALIFORNIA 94720